Desalination and Water Treatment
www.deswater.com

doi: 10.5004/dwt.2022.28329

254 (2022) 260–273
April

Comparative study on adsorptive efficiency assessment of Congo red dye from aqueous solutions using nanoporous zirconia oxides and anionic clays nanosheet

Fatiha Boukraa Djellal Saïah*, Noureddine Bettahar

Laboratory of Inorganics Materials Chemistry and Applications (LCMIA), University of Sciences and Technology of Oran "Mohamed Boudiaf" (USTO.MB), B.P. 1505 El Menaouer, Oran 31000, Algeria, Tel. (+213) 7 90 54 01 63; emails: f_boukraa2003@yahoo.fr (F.B. Djellal Saïah), nbettahar2001@yahoo.fr (N. Bettahar)

Received 6 June 2021; Accepted 19 February 2022

ABSTRACT

The approach of this study was the assessment of the dye sorption performance on hierarchical porous zirconium oxide ZrO_2 as compared to the performance as decontaminant of various uncalcined anionic clays layered double hydroxide (LDH) and calcined clay. The aim of the work was also to propose probable adsorption mechanisms and interactions between the pollutant and surface of these materials. The LDHs materials, with molar ratios of 3:1 (M^{2+}/M^{3+} = 3), were obtained by co-precipitation method. The ZrO_2 nanoparticles were synthesized by a sol–gel process with the aid of a structure-directing surfactant. The obtained materials were characterized by X-ray diffraction, Fourier-transform infrared spectra, Brunauer–Emmett–Teller, transmission electron microscopy, scanning electron microscopy, thermogravimetric/Differential Scanning Calorimetry and pH of zero point charge (pH_{pzc}) measurements. Elimination of acidic dye as a function of contacting time was studied. The adsorption was evaluated in the removal of Congo red (CR) from simulated wastewater. These results were compared with tests performed with Ni–X and Co–X (X = Fe and Al) LDHs, the calcined product of Ni–Fe (denoted CNiFe) and the zirconia oxide. All materials seems to have an affinity toward CR dye molecules in aqueous solution. Furthermore, the adsorption was more effective on calcined LDH clays than original precursors. The as-prepared zirconium oxides would be regarded as more effective adsorbents for the removal of acidic dye in wastewater treatment. The enhanced adsorption capacity of the zirconium oxide revealed that high specific surface area and hierarchical pore structure increases the active adsorption sites and promotes the interactions between the adsorbent and CR dye via electrostatic interactions, hydrogen bonding and may be trapped inside the pores.

Keywords: Synthesis; Characterization; Anionic clays; Zirconia oxide; Congo red removal

1. Introduction

There is a current need to treat dye-containing effluents prior to their discharge as these compounds and their degradation products can be toxic at low concentrations. Various types of dyes are manufactured for printing and dyeing industries from coal tar based hydrocarbons. These industries are major water consumer and cause water pollution. Congo red is an example of diazo dyes and is red in the pH range of 5–10. Adsorption is an attractive method for the elimination of contaminants from effluents. Although activated carbon remains the most widely used adsorbent, its relatively high cost restricts its use somewhat [1]. However, in addition to cost, availability and adsorptive properties are also criteria when it comes

* Corresponding author.

to choosing an adsorbent for depollution, thereby encouraging research into compounds that are both efficient and cheap. Indeed, several authors have reported the use of various kinds of adsorbents including activated carbon [2], clay [3], biomaterials [4], composite [5] and fly ash [6] have been investigated and found to be capable of removing the dyes from wastewater. In term of cost, ease of operation, clays materials have been considered as the most appropriate sorbents [7–9]. Layered double hydroxide (LDH), based on the unique anion exchange property [10–12], has received interest for the environmental remediation [13,14]. LDH consists of positively charged brucite-like hydroxide sheets, with suitable cations incorporated, alternating with negatively charged inter layers containing anions and water molecules [15]. The general formula of LDH is $(M^{2+}_{1-x}\ M^{3+}_{x}\ (OH)_2)^{x+}\ (A^{n-}_{x/n})$. nH_2O, where M^{2+} and M^{3+} can be any divalent and trivalent cation in the octahedral positions within the hydroxide layers: $M^{2+} = Mg^{2+}$, Zn^{2+}, Ni^{2+}, $M^{3+} = Al^{3+}$, Cr^{3+} or Fe^{3+} [16] etc., and A^{n-} is an interfoliar anion [17]. The metal ratios $x = M^{3+}/M^{2+}+M^{3+}$ variable ($0.2 < x < 0.3$). The hydroxide sheets are positively charged and require intercalation of anions such as CO_3^{2-}, NO_3^-, SO_{40}^{2-} or Cl^- to remain the overall charge neutrality [10,18,19]. However, their applications is influenced by optimum physicochemical properties in particular by crystallinity, morphology and particle size [20,21]. The most important characteristics of the LDH material is its memory effect. When heated to 250°C–600°C, some LDH can be converted into mixed metal oxides, and the calcined products might reconstruct the original layered structure in a solution containing intercalation anions [22–24]. This property of the calcined-layered double hydroxide (CLDH) is called ''memory effect'' [25]. The CLDH material has attracted more attentions in the environmental research field because of its thermal regeneration procedure and high anion retention capacity [26,27]. Porous materials have been widely used to prevent environmental pollution from industrial wastewater [28–30] such as transition metals oxides. These materials, have been considered as an important materials used for a various applications [31]. It can be applied as catalysts [32,33], catalyst supports [34,35] photocatalytic materials [36,37], and chemical sensors [38,39]. With the aim of improving the efficiency of use, introducing a multi porosity structure to zirconia oxide nanoparticles has been prepared as a potential route [40]. These structures possess high surface areas. They have been used as adsorbents [31] and catalysts. In particular, mesostructured zirconia oxides [41,43,44] have been investigated as adsorbents for the elimination of anionic and cationic pollutants from effluents. Several research have been carried out on the effects of structural properties on the sorption of pollutants on zirconia [45,46], heavy metals [47,48], and organic molecules [49,50]. Hierarchically porous metal oxides have been prepared by an emulsion templating strategy [51–54]. Other hierarchically porous structures in Al_2O_3 [55], ZrO_2 [56–58], TiO_2 [59] and aluminosilicates [60] have been realised by a one pot synthesis using one type of surfactant molecules and a metal alkoxide precursor. In zirconia synthesis, the precursors zirconium n-butoxide [31] and zirconium n-propoxide [61] are used. pH_{pzc} is called as the pH for which the material under consideration has neutral charge. The most significant quality of pH_{pzc} is that the material has a positive charge below pzc pH and negative charge beyond pzc pH. This unique feature of having positive and negative charge allows anions and cations to be adsorbed on the surface. The use of clays and oxides as precursor for adsorption will provide solution to environmental problems caused by wastes. In the present study, experiments have been performed for the removal of Congo red (CR) dye using adsorption techniques. Some synthetic adsorbents such as transition metal based anionic clays (LDHs) and their calcined product (CLDH) compared with hierarchically nanoporous zirconia oxide have been selected. The pH of the point of zero charge of all materials was determinated by pH drift method at room temperature. Also discussed is a proposed adsorption mechanism.

2. Materials and methods

2.1. Adsorbate (dye preparation)

Congo red dye was the sodium salts of acide benzidinediazo-bis-; 1-naphthylamine-4-sulfonic with a formula $C_{32}H_{22}N_6Na_2O_6S_2$, has a Mw = 696.67 g/mol, was supplied by Sigma-Aldrich with 99.99% purity, was used as received and its chemical structure is shown in Fig. 1.

A Congo red dye (1.0 g) was dissolved per 1 L of distilled water to prepare 1 g/L of CR stock solution. Serial dilutions were made by diluting the dye stock solution in accurate proportions to the desired concentrations. The calibration curve for the CR dye was prepared by recording the absorbance values for a range of known concentrations of dye solutions (5–30 mg/L) at the wavelength of maximum absorbance λ_{max} = 500 nm. UV-visible spectroscopy is used to determine the amount of residual CR dye in solutions.

2.2. Sorbents reactants

All reactants used in this work have high purity degree and were from Sigma-Aldrich. The various chloride salts $NiCl_2{\cdot}6H_2O$, $FeCl_3{\cdot}6H_2O$, $CoCl_2{\cdot}6H_2O$, $Al(Cl)_3{\cdot}6H_2O$, (Acros, 99%), NaOH (Acros, >97%) and Na_2CO_3 were used. The liquid precursor zirconium alkoxide $[(Zr(OC_4H_8)_4]$: zirconium n-butoxide (80% solution in 1-butanol, Aldrich), was used as purchased with surfactant (Brij 56, decaoxyethylenecetyl ether, alkyltrimethylammonium: $(C_{16}(EO)_{10})$.

2.3. Sorbents preparation

2.3.1. LDHs and CLDH precursors preparation

A series of metal transition containing layered double hydroxides type Co–X and Ni–X (X = Fe^{3+} and Al^{3+}), with

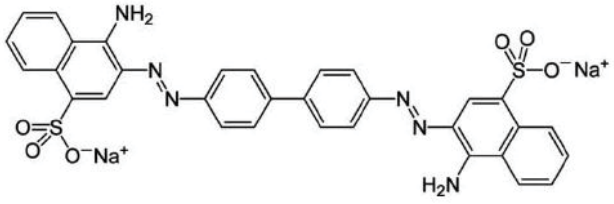

Fig. 1. Chemical structure of Congo red (CR) dye.

molar ratio M^{2+}/M^{3+} of 3/1 were prepared by co-precipitation method. The anionic clays were obtained by dropwise adding, at room temperature, a solution containing mixed chloride of the divalent (0.75 M) and trivalent (0.25 M) metals dissolved in 250 mL of distilled water to a vigorously stirred solution (250 mL) containing NaOH (1 M) and Na_2CO_3 (2 M) at constant pH = 10. The resulting slurries were stirred mechanically for a further 1 h at room temperature and constant pH value. The suspensions were then transferred into the Teflon coated stainless steel autoclave to undergo hydrothermal treatment at 393 K for 24 h, in order to obtain better crystallized materials. The precipitate formed was filtered and washed several time with distilled water. Then the materials were dried in an oven at 353 K overnight and were denoted $M^{2+}M^{3+}CO_3$. A fraction of the obtained $NiFeCO_3$ LDH was calcined at 593 K during 2 h in an air atmosphere with heating and cooling rates of 2°C/min. The obtained solid was designated as CNiFe. Both the calcined and uncalcined LDH were ground prior to analysis and use in adsorption.

2.3.2. Porous zirconia preparation

The preparations of the macro-mesoporous zirconia oxide are processed by the method described elsewhere [55–57]. Briefly, 15 wt.% micellar solution of Brij 56 ($C_{16}(EO)_{10}$), is prepared by dissolving this latter in an aqueous acidic solution (pH = 2) at 313 K under stirring for 3 h. An appropriated amount of zirconium n-butoxide ($Zr(OC_4H_9)_4$ is added dropwise into the above solution with a surfactant: Zr molar ratio of 0.33 and 1.65. After further stirring for 1 h, the mixture is transferred into a Teflon lined autoclave, and heated at 333 K for 48 h. The product is filtered by Soxhlet extraction with ethanol for at least 36 h in order to remove the surfactant species and then dried at 333 K. The obtained materials denoted respectively as CMI7Zr0.33 and CMI7Zr1.65.

2.4. Point zero charge analysis

The value of the pH necessary to affect a net zero charge on a solid surface in the absence of specific sorption is called the point of zero charge (pH_{pzc}). The pH_{pzc} of all materials was measured by pH drift method [62,63]. The pH at pH_{pzc} was determined in NaCl solutions (inert electrolytes) with different concentrations. The initial pH value of NaCl solution was adjusted to cover range from 2 to 12 by adding 0.1 M HCl and 0.1 M NaOH. Then 25 mL of 0.01 M NaCl is taken in flasks and 25 mg of adsorbent is added to each solution. The suspensions were then sealed and shaken for 48 h at 150 rpm and at room temperature. The final pH values of the supernatant liquid were noted. The difference (ΔpH) between the initial pH (pH_i) and final pH (pH_f) values ($\Delta pH = pH_i - pH_f$) was plotted against the values of pH_i. The point of intersection of the resulting curve with abscissa, gave the pH_{pzc}. The pH_{pzc} is the point where $pH_i - pH_f = 0$.

2.5. Sorption experiments

Batch adsorption experiments were performed at ambient temperature and pH of the dye solutions (pH = 6–7). A sorption kinetic study of the CR dye on various obtained LDHs and on zirconia oxides were carried out by dispersing 250 mg of each material into 100 mL of CR solution with an initial concentration of 100 mg/L at normal pH. The adsorption experiments were carried out for different contact time in the range of 0–3 h. The mixture was stirred at 150 rpm. 5 mL of suspension were extracted at selected time, and separated by centrifugation at 2,500 rpm for 10 min. The residual concentrations were determined by using a UV-Vis spectrometer at λ_{max} = 500 nm. The efficiency for Congo red removal from the suspension (*R*% vs. time) was calculated using the following equation:

$$R\% = \left(\frac{C_0 - C_t}{C_0}\right) \times 100 \quad (1)$$

where C_0 and C_t are the initial and the equilibrium CR concentrations in mg/L, respectively.

2.6. Materials characterization

Powder X-ray diffraction patterns (XRD) of synthesized materials were recorded using Philips PW1820 diffractometer using Cu Ka radiation (λ = 1.5418 Å, 30 kV, 40 mA, step 0.02° 2θ, time 1s) over a 2θ range of 4°–70°. Identifications of the crystalline phases were done by comparison with the JCPDS files [64]. FT-infrared spectra of materials were recorded using KBr pellets technique in a Perkin-Elmer FTIR 2000 spectrometer in the range of 4,000–400 cm^{-1}. Nitrogen adsorption–desorption isotherms were collected at 77 K over a wide relative pressure range from 0.01 to 0.995 with a volumetric adsorption analyzer TRISTAR 3000 manufactured by Micromeritics. The pore diameter and the pore size distribution were determined by the BJH method [65]. Thermogravimetric/Differential Scanning Calorimetry (TG/DSC) of these materials was carried out using Seteram TG-DSC 111 equipment, in the temperature range between 293 and 1,073 K at a heating rate of 5°C/min^{-1} under a nitrogen atmosphere. The morphology of the obtained phases was studied using Philips XL-20 scanning electron microscopy (SEM) at 20 keV. Electron micrographs of the samples were taken by the transmission electron microscopy (TEM) on Philips TECNAI-10 instrument at 80 keV. Ultraviolet-visible (UV-Vis) adsorption spectra were collected on a Perkin-Elmer Lambda 35 spectrometer.

3. Results and discussion

3.1. XRD analysis

3.1.1. Characterization of LDH and CLDH

Fig. 2 shows the powder X-ray diffraction patterns of the prepared LDHs materials. The patterns of all samples showed the diffraction lines typical for hydrotalcite structure with interlayer carbonate [18]. It can be found that the LDH materials showed a layered structure with symmetric reflections of basal (003), (006) (strong peaks, narrow and symmetric, at low 2θ values), and (009) planes, broad asymmetric reflections of basal (015) and (018) planes, followed by two small peaks (110) and (113) corresponding to the characteristic peaks at 2θ = 60° and 62° [27]. The unit

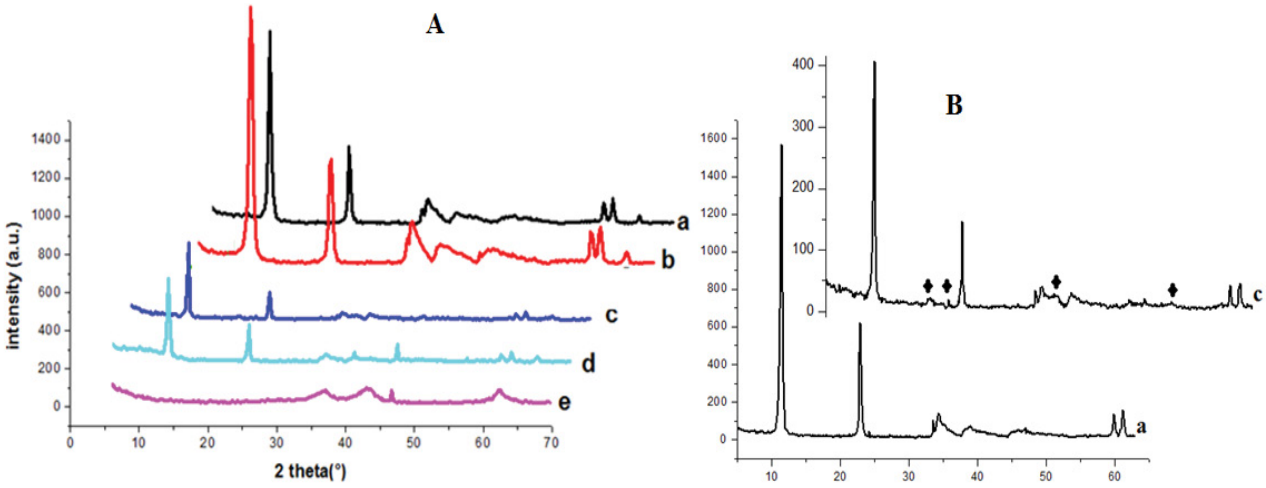

Fig. 2. XRD patterns of LDHs samples (A): (a) $NiFeCO_3$, (b) $NiAlCO_3$, (c) $CoFeCO_3$, (d) $CoAlCO_3$, (e) CNiFe. (B): (a) $NiFeCO_3$, (c) $CoFeCO_3$, ♦ additional phases not identified.

cell parameters *c* and *a* (Table 1), were obtained by Bragg's law, assuming hexagonal stacking. "*a*" was obtained from the position of the (110) peak as $a = 2d(110)$, and "*c*" was calculated from the position of the first basal (003) peak as $c = 3d(003)$. However, not all metal combinations led to the formation of a pure LDH phase as shown in Fig. 2Bc, for XRD pattern of Co and Fe containing LDH. These later showed additional phases. The diffractions lines become weaker and less defined (Fig. 2Bc). In contrast, with the samples $NiFeCO_3$ and $NiAlCO_3$ LDHs (Fig. 2Aa,b), It is observed that the parameter "*c*" values increased with increasing *d*-spacing as shown in Table 1 and the (003) reflection is sharp indicating an improved crystallinity. The lower intensity of the peaks can be related to a worse crystallinity of the samples [20] as shown in Fig. 2Bc. Such behaviors indicate structures poorly ordered along the *c* axis. The XRD patterns in Fig. 2Ae shows three broad reflections indicating that the layered structure of CNiFe is destroyed by heating it at 593 K, resulting in mixed oxide.

Table 1
Unit cell parameters distance of the LDHs phases

Samples	*d*(003)	*c*	*a*
	(Å)	(Å)	(Å)
$NiFeCO_3$	7.82	23.51	3.09
$NiAlCO_3$	7.73	23.17	3.05
$CoAlCO_3$	7.73	23.17	3.09
$CoFeCO_3$	7.65	22.93	3.12

3.1.2. Characterization of zirconia oxide

XRD patterns of meso-macroporous zirconia oxide are shown in Fig. 3. The wide-angle XRD patterns reveal an amorphous zirconia framework. No distinction can be made between the samples with the two surfactant: Zr ratio 0.33 and 1.65.

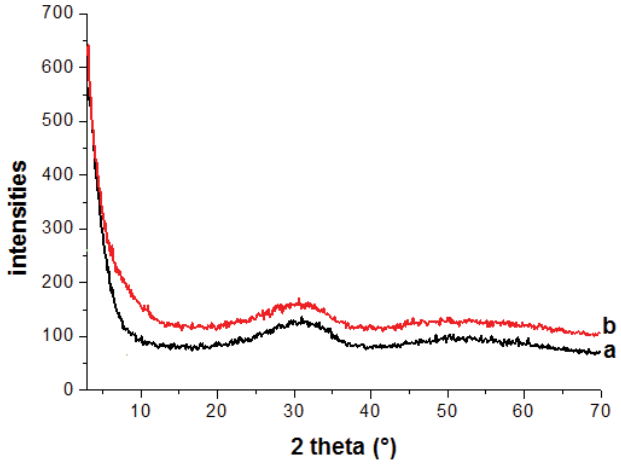

Fig. 3. XRD patterns of zirconia oxides samples: (a) CMI7Zr0.33 and (b) CMI7Zr1.65.

3.2. Infrared analysis Fourier-transform infrared spectroscopy

3.2.1. Characterization of LDH and CLDH

The Fourier-transform infrared (FTIR) spectra of LDHs samples are shown in Fig. 4a. It resembles that of other carbonated hydrotalcite-like phases [21,29,30]. It showed a broad and strong band in the range 3,000–4,000 cm^{-1} (Fig. 4a), three broad and intense bands are observed, which are attributed to the vibrations of the structural OH^- groups, vibrations of physisorbed water, or characteristic stretching vibrations of M–OH in hydroxycarbonates. The ϑH–O–H bending and ϑO–H symmetric bands appeared at 1,640 and 3,440–3,490 cm^{-1}, respectively [47]. A sharp and symmetric band at 1,364 cm^{-1} was attributed to symmetric carbonate stretching. The absorption bands below 1,000 cm^{-1} were Metal-O vibration modes of LDH. The FTIR spectra of $CoFeCO_3$ (Fig. 4a) had presence of low vibration band at 3,650 cm^{-1}. This indicated that not all OH group is held

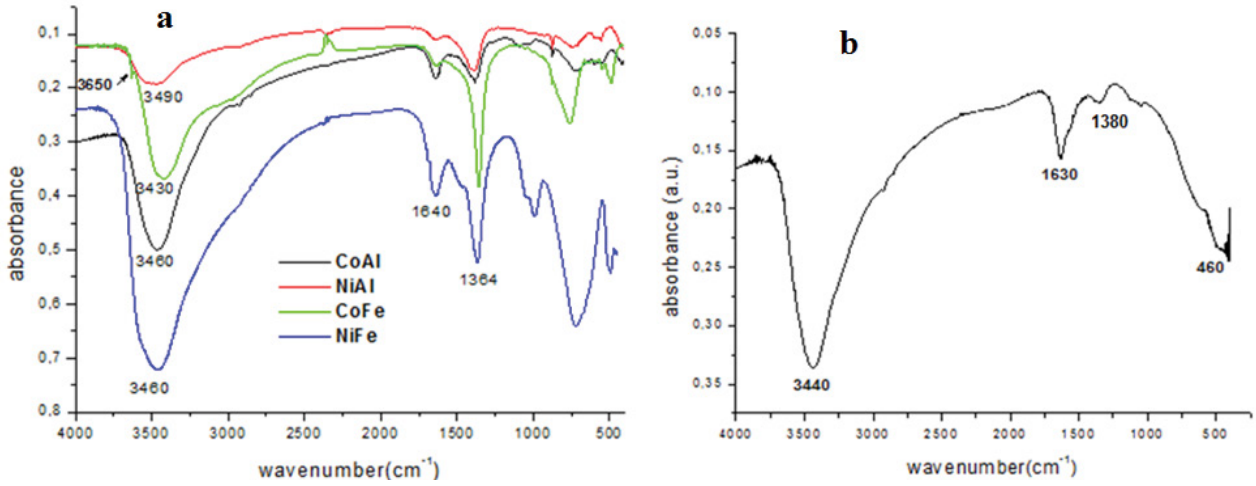

Fig. 4. FTIR spectra of: (a) LDHs samples and (b) CMI7Zr0.33.

through hydrogen bonding but can be presented as free both in the network and in interlayer water molecules.

3.2.2. Characterization of ziconia oxide

Fig. 4b shows the FTIR spectra of zirconium oxide, CMI7Zr0.33. The FTIR spectrum of the two samples showed similar bands. The very broad absorption band at 3,440 and 1,630 cm^{-1} are assignable to OH vibrations of adsorbed water molecules. The peak at 1,380 is assignable to Zr-OH vibrations. The peak at 460 cm^{-1} is assignable to Zr-O vibrations.

3.3. Textural and structural properties

3.3.1. Characterization of LDH and CLDH

Nitrogen adsorption–desorption isotherms of LDHs materials measured at –196°C are shown in Fig. 5 and the results of surface area measurements are included in Table 2. The shape of all isotherms are type II according to the IUPAC classification [65] and this behaviour can be also explained by the existence of spaces between particles of nanometric size thus forming an interparticle porosity. Desorption started immediately after completion of the adsorption, which show a narrow hysteresis loop, corresponding to type H3, ascribed to mesopores open at both ends. For the samples $NiAlCO_3$ (Fig. 5b), the loops closed around 0.7 relative pressures (P/P_0) with a small plateau at high P/P_0, which attributes to the mesoporous nature of these samples. This latter showed an increasing in the width of the hysteresis loop leading to formation of small intraparticle pores (Fig. 5b). For the samples $NiFeCO_3$, $CoFeCO_3$, $CoAlCO_3$ and CNiFe (Fig. 5a, c, d and e), the hysteresis loop closed at P/P_0 around 0.85 and 0.9. These results indicated that these compounds had smaller mesopores than $NiAlCO_3$. Hysteresis loops which exhibit no limiting sorption at high pressure, are almost vertical and parallel at high relative pressure (Fig. 5a, c, d and e) and such shape of the loops suggests to nonuniform size with plate-like aggregated particles leading to slit-shaped pores of the hydrotalcite material [20]. The value of average pore volume and surface area for these samples are given in Table 2. The Brunauer–Emmett–Teller (BET) surface area of calcined samples CNiFe increased assuming that removal of water molecule and carbon dioxide from carbonate in the interlayer during calcination leads to formation of channels and pores, thus accounting for the increase in specific surface area [66]. This sample presented an abrupt increase in the nitrogen adsorbed volume (Fig. 5e). These results are confirmed from the analysis of the transmission electron microscopy in Fig. 6e. The structure of calcined sample demonstrates highly porous crystallites with different sizes (Fig. 6e).

Table 2
Textural properties of the LDHs, CLDH and zirconia oxides

Samples	S_{BET} [a]	V_p [b]	D_p [c]
	(m^2/g)	(cm^3/g)	(nm)
$CoAlCO_3$	33	0.30	36.9
$CoFeCO_3$	54	0.23	17.4
$NiAlCO_3$	85	0.34	15.9
$NiFeCO_3$	79	0.48	24.0
CNiFe	156	0.27	6.50
CMI7Zr1.65	634	0.42	2.65
CMI7Zr0.33	519	0.47	3.24

[a]BET surface area,
[b]Porous volume determined from N_2 uptake at $P/P_0 = 0.99$,
[c]Porous diameter.

The TEM micrographs shows the morphology of regular hexagonal plates (Fig. 6), with a thin and wide nature of the LDH, characteristic of hydrotalcite-like compounds (HT) [20,51]. No amorphous phase was noticed in TEM micrographs for LDH samples indicating the formation of single LDH phase. Except for $CoFeCO_3$ sample which was detected spherical particle at low amount and are surrounded in Fig. 6c. These results confirm fully the XRD and BET results. The average size of the lamellar thin hexagonal particles was varied from 100 to 500 nm.

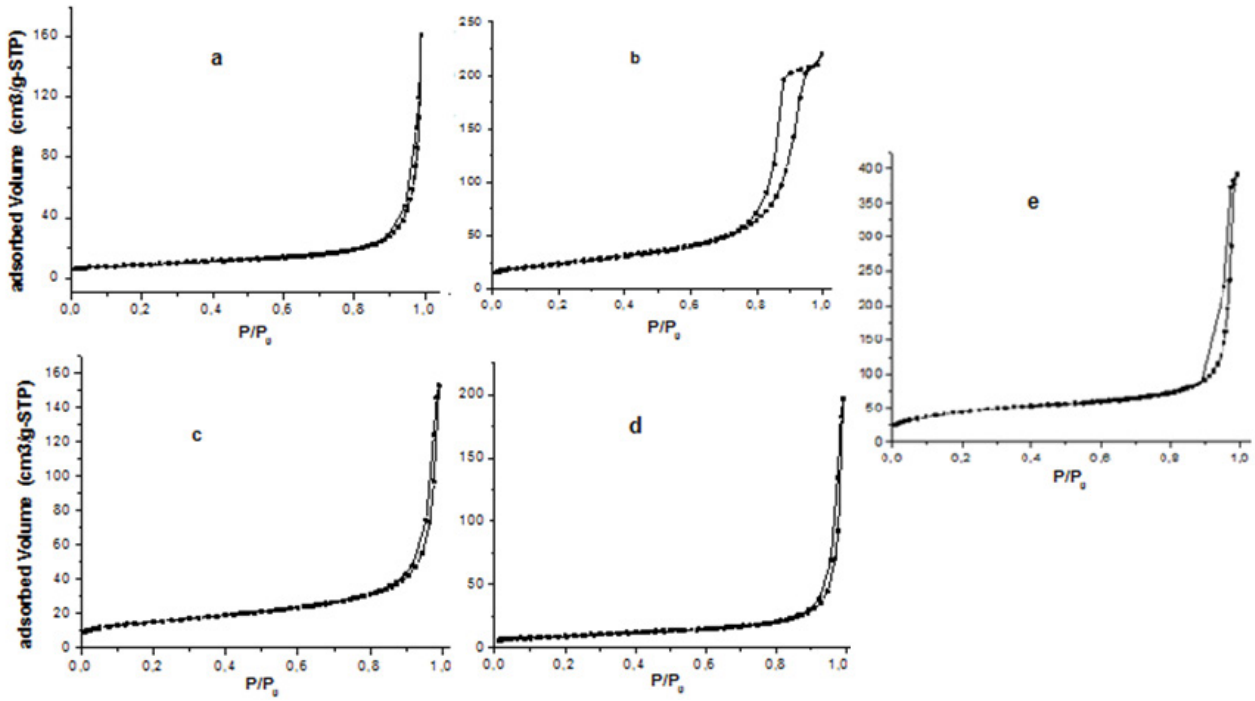

Fig. 5. Nitrogen adsorption–desorption isotherm at 77K for: (a) $NiFeCO_3$, (b) $NiAlCO_3$, (c) $CoFeCO_3$, (d) $CoAlCO_3$, and (e) CNiFe.

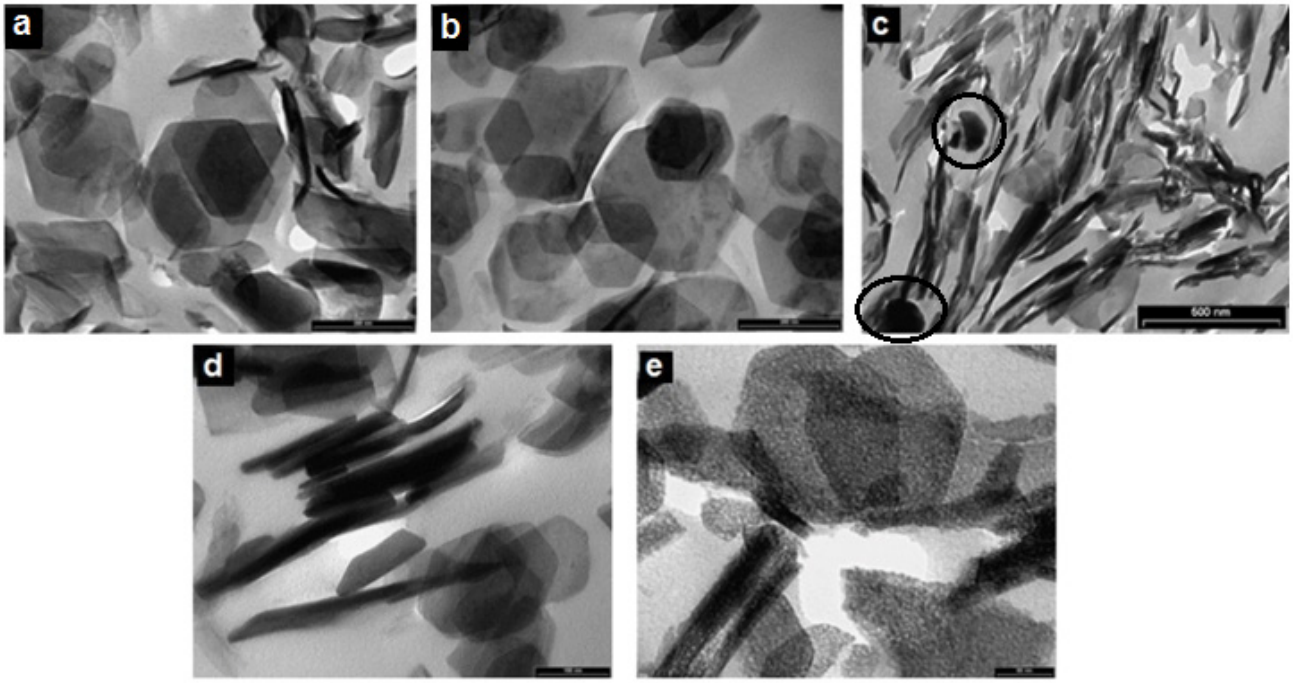

Fig. 6. TEM micrographs of LDHs materials: (a) $NiFeCO_3$, (b) $NiAlCO_3$, (c) $CoFeCO_3$, (d) $CoAlCO_3$, and (e) CNiFe.

Scanning electron micrographs (SEM) of LDHs materials showed well crystallised materials with hexagonal platelets (Fig. 7). It can be observed agglomerated thin spherical-to-hexagonal flat crystals in a layered structure of $NiAlCO_3$ LDH (Fig. 7b), which leads to formation of small intraparticle pores, by comparison with aggregates of small particles for $NiFeCO_3$ sample (Fig. 7a). These results confirm fully the BET results. In addition, the SEM images of the samples CNiFe (Fig. 7e) showed agglomeration of primary particles [20]. It's probably results from disordered staking of the particles due to the calcination temperature.

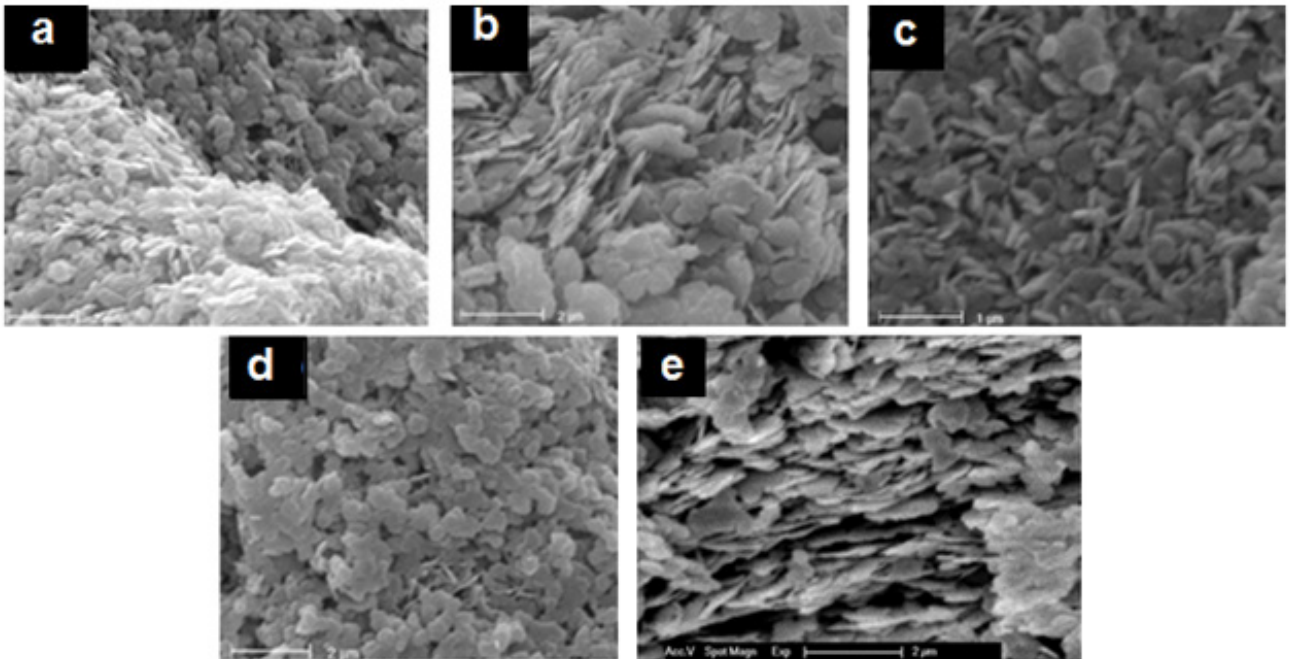

Fig. 7. SEM micrographs of LDHs materials: (a) $NiFeCO_3$, (b) $NiAlCO_3$, (c) $CoFeCO_3$, (d) $CoAlCO_3$, and (e) CNiFe.

3.3.2. Characterization of zirconia oxide

Fig. 8 shows TEM, SEM images and nitrogen adsorption–desorption isotherms of the obtained oxides. The isotherms of nitrogen adsorption–desorption and the corresponding BJH pore size distribution curves (inset) of meso-macroporous zirconia are shown in Fig. 8a and b. It is seen from the isotherm that a strong uptake of N_2 due to capillary condensation occurs in a relative pressure (P/P_0) range of 0.10–0.40 and reaches a plateau at P/P_0 range of 0.60–0.90. This kind of isotherm indicates that the material belongs to the mesoporous family with the pore size ranging of 1.0–2.0 nm. The pore size distribution curve obtained by the BJH method using the adsorption branch of the isotherm is centered at about 1.33 and 1.37 nm for CMI7Zr0.33 and CMI7Zr1.65 respectively (Fig. 8a and b). The BET surface area is 519 and 634 m^2/g with a pore volume of 0.47 and 0.42 cm^3/g, respectively. The results are represented in Table 2. A SEM was used to examine the surface of the prepared adsorbents. Fig. 8c shows the SEM photographs of zirconia oxide. The zirconium oxides are meso-macroporous, with an amorphous structural framework (Fig. 8c). It has been shown that these oxides exhibit well-defined macropores with interconnected mesopores constructed by zirconium nanoparticles (Fig. 8d and e). These later formed macrochannels parallel to each other (Fig. 8c) [45,46]. The TEM images also revealed the presence of macropores (Fig. 8d) with disordered mesoporous walls (Fig. 8d and e).

3.4. Thermal analysis

3.4.1. Characterization of LDH and CLDH

Fig. 9 shows a typical DTA/TG thermogram of the LDHs materials. The thermogravimetric and differential thermal analysis (TG-DTA) of LDHs samples ($NiFeCO_3$, $NiAlCO_3$, $CoFeCO_3$, and $CoAlCO_3$) shows that in each case the weight loss occurs essentially in two steps below 500°C. Two prominent endothermics peaks are seen in the DTA curve (Fig. 9). An endothermic peak relating to the dehydration of the physisorbed water molecules from the external surface of the LDHs was noticed in the temperature 209°C for $NiFeCO_3$, 250°C for $NiAlCO_3$, 195°C for $CoFeCO_3$, and 220°C for $CoAlCO_3$ as shown in Fig. 9a–d, respectively. The second region, ranging from 250°C to 450°C corresponded to the weight loss due to the dehydroxylation and de-carbonation reactions. This later peak is due to formation of metal oxides and there is no substantial weight loss observed above 450°C. The low temperature peak recorded at 100°C–250°C in the derivative thermogravimetric (DTG) curves, which is related to the loss of interlayer water, shifts to lower temperatures for $CoFeCO_3$ LDH (195°C) (Fig. 9c). This is indicative of a decrease in the strength of hydrogen bond between water molecules and interlayer CO_3^{2-} ions. This was a consequence of the decrease in the crystallinity of LDH sample. DTA/TG thermogram of the $CoFeCO_3$ LDH shows a low weightloss at 355°C probably due to oxidation of amorphous phase. On the contrary, for $NiAlCO_3$ LDH the first peak was noticed in the temperature 250°C (Fig. 9b), which indicated an increase in the strength of hydrogen bond between water molecules and interlayer CO_2^{-3} ions. This is indicative of more crystalline phase. These results confirm fully the XRD, BET and TEM results. The second DTG peak of the LDH samples was noticed in the temperature 310°C for $NiFeCO_3$, 355°C for $NiAlCO_3$, 270°C for $CoFeCO_3$, and 250°C for $CoAlCO_3$ as shown in Fig. 9a–d, respectively. This indicated a higher temperature of 355°C and 310°C for $NiAlCO_3$ and $NiFeCO_3$ LDHs respectively, due to increasing interaction between the layers and the CO_2^{-3} ions. This provided evidence of structures more ordered. These results confirm the XRD interpretations.

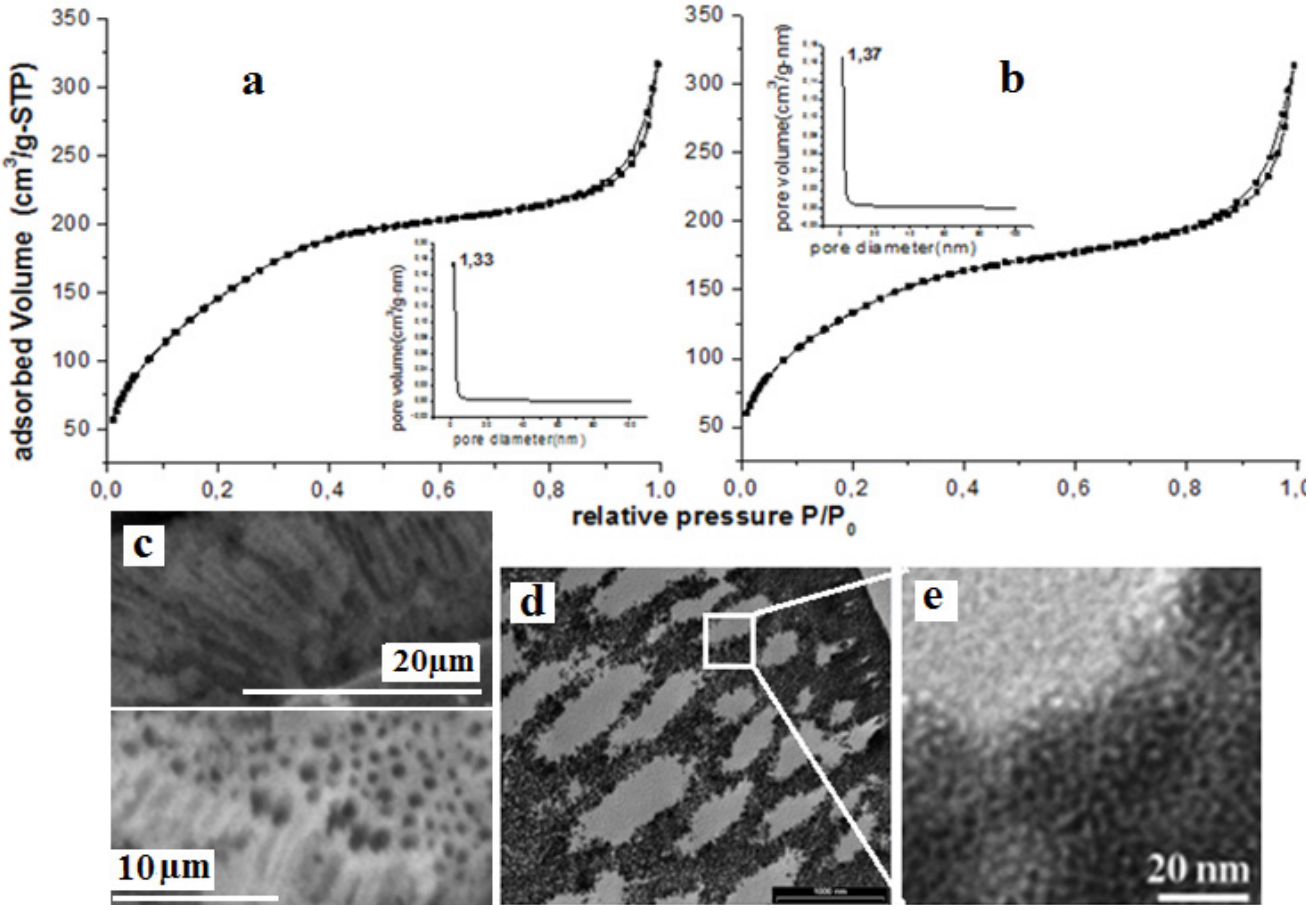

Fig. 8. (a, b) Nitrogen adsorption–desorption isotherm and the corresponding pore size distribution curve (inset) of CMI7Zr0.33 and CMI7Zr1.65, respectively. (c) SEM images of meso-macroporous zirconium oxides. (d) Low magnification TEM images of the macropores viewed side-on to the pores; (e) a higher magnification image of the macropores walls showing the mesophase.

However, the thermal stability is relatively greater for $NiAlCO_3$ and $NiFeCO_3$ to that of $CoAlCO_3$ and $CoFeCO_3$.

3.4.2. Characterization of zirconia oxide

The thermogravimetric and differential thermal analysis (TG-DTA) of the structural properties of the sample were also studied by thermogravimetry. Fig. 10 shows the weight loss during the thermal treatment of macro-mesoporous material CMI7Zr0.33 and CMI7Zr1.65 (Fig. 10a and b). This thermogram can be divided into three parts. Firstly, between 25°C and 150°C, an initial mass loss associated with an endothermic effect is attributed to the desorption of water physisorbed at the surface of the material. Then, between 150°C and 350°C, a second less significant mass loss with an exothermic effect corresponds to the destruction of the Zr-OH bonds and formation of Zr-O-Zr bonds. The weight loss at temperatures from 200°C to 320°C (Fig. 10a) and from 200°C to 350°C (Fig. 10b), accompanied by an exothermic peak corresponds to the oxidation of the residual ethanol or the surfactant. A second exothermic peak from 400°C to 500°C was observed without weight loss. This peak is attributed to the crystallization of the amorphous zirconia.

3.5. Adsorption performance of materials

3.5.1. Effect of pH (pH_{pzc})

The pH of the solution is one of the most important factors controlling the removal of pollutants from wastewater by adsorption. It affects the nature of the surface charge of the materials as-well-as the ionization of the aqueous pollutant species, the degree of dissociation of functional groups from the active sites of the adsorbent and consequently the rate of adsorption [67]. Congo red is a dipolar molecular. It exists as anionic form at basic pH (6–10) (Fig. 11A) with the main red color and as cationic form at acidic pH (3–5) with dark blue color (Fig. 11B) [68]. The CR in aqueous solution is red in pH values more than ten. This red color was found to be different than the original red color [69]. According to the molecular diagram of CR illustrated in Fig. 11, it's sulfonic ($–SO_3$) bond represents its most reactive component. The results for the determination of pH_{pzc} are shown in Fig. 12. As displayed in Fig. 12, the pH_{pzc} values are approximately 6.3, 7.2, 8.4, 6.9, 8.2 and 7 for CMI7Zr1.65, $NiFeCO_3$, $NiAlCO_3$, $CoFeCO_3$ $CoAlCO_3$ and CNiFe, respectively. Therefore, there was a negatively charged surface of materials at pH over these values while there was a positively charged surface of materials at pH

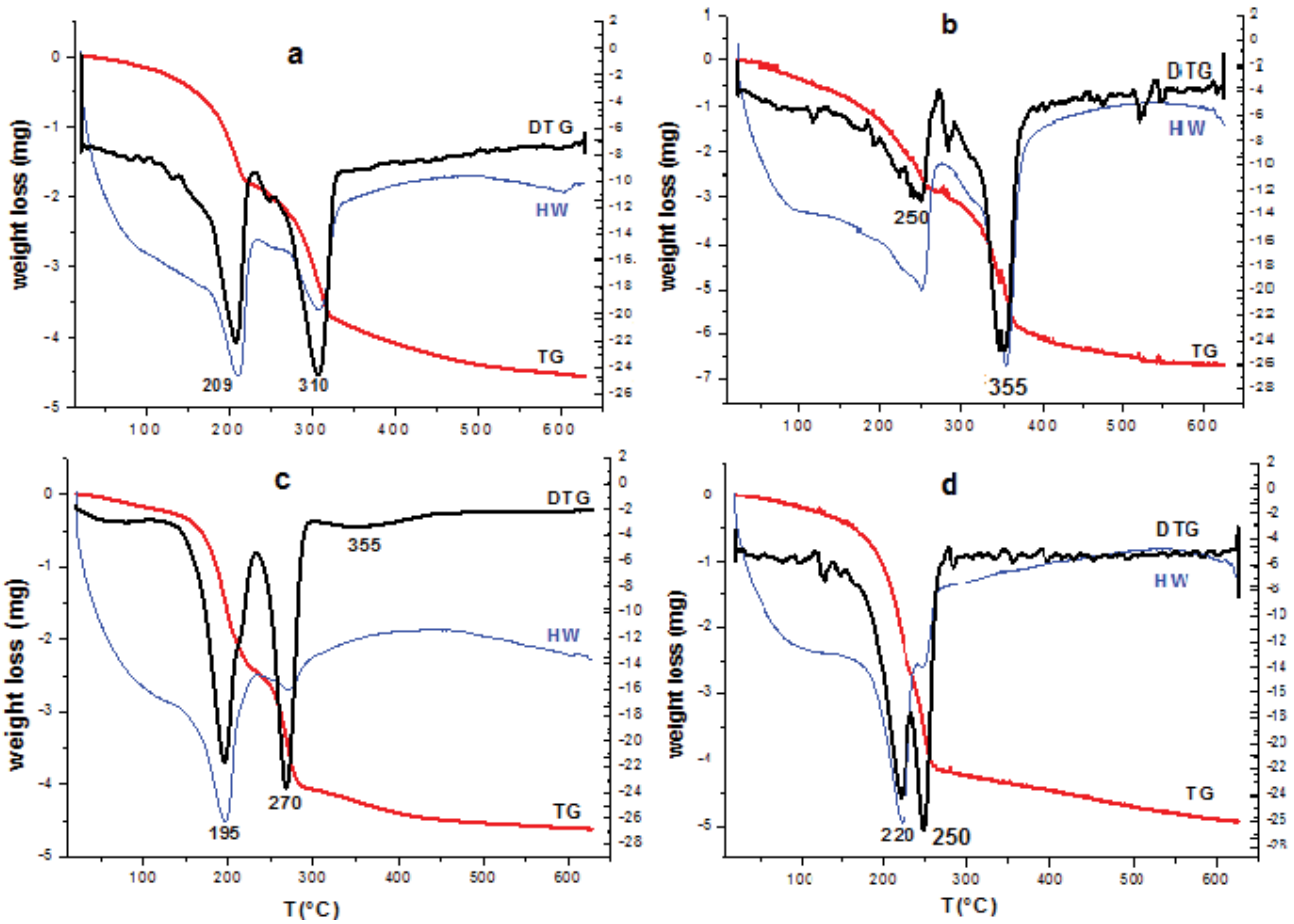

Fig. 9. TG-DTG curves of LDHs: (a) $NiFeCO_3$, (b) $NiAlCO_3$, (c) $CoFeCO_3$, and (d) $CoAlCO_3$.

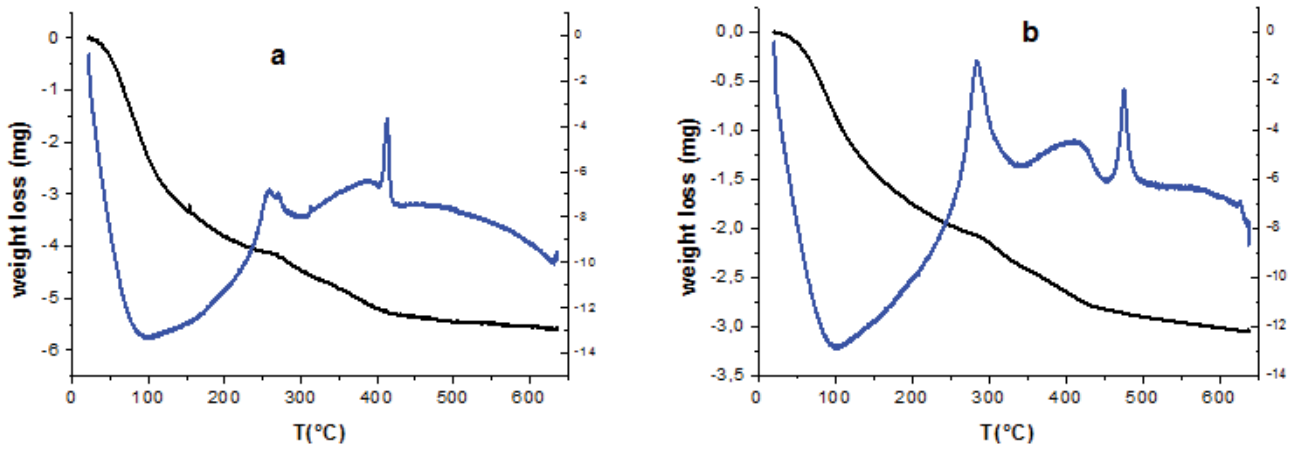

Fig. 10. TG-DTG curves of meso-macroporous zirconium oxides: (a) CMI7Zr0.33 and (b) CMI7Zr1.65.

below these values. This reveals that at pH < pH_{pzc}, the surface of the adsorbent favors the adsorption of anionic species, which in this case is CR. While, at pH > pH_{pzc}, the surface of the adsorbent favors the adsorption of cationic species due to electrostatic interactions [70].

3.5.2. Effect of contact time

The experiments were carried out in order to test the performance of removal CR by adsorption on these samples according to their structural and textural properties.

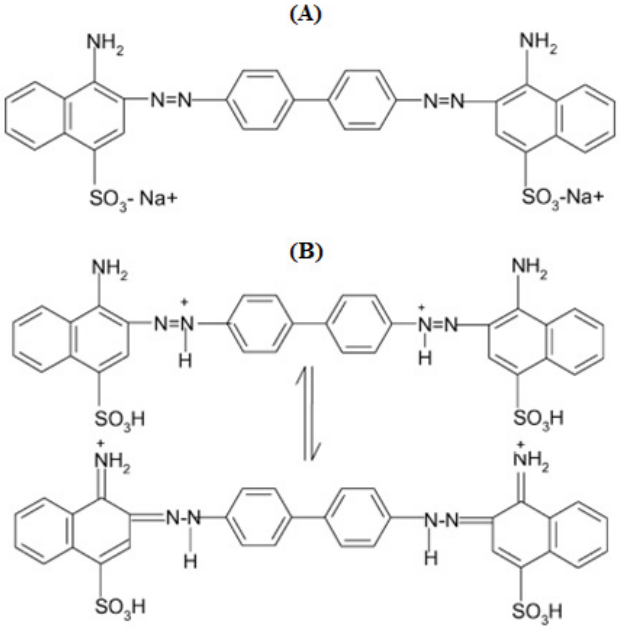

Fig. 11. Structure of Congo red at (A) pH > 5.5 and (B) pH < 5.5.

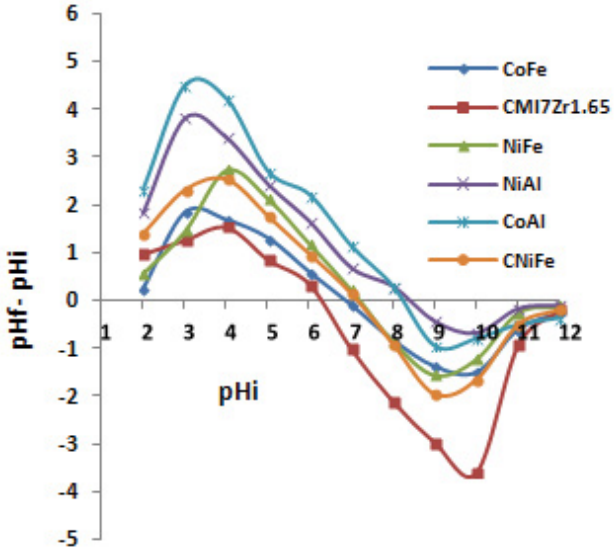

Fig. 12. Zero point charge (pH_{pzc}) graphs for synthesized materials.

Effect of sorption time on CR removal by $NiFeCO_3$, $NiAlCO_3$, $CoFeCO_3$, $CoAlCO_3$ LDHs, CNiFe and zirconia oxides CMI7Zr0.33 and CMI7Zr1.65 was examinated (Figs. 13 and 14). Eq. (1) was used to calculate the color removal efficiency in the treatment experiment. It was found that the CR removal percent increased with increasing contact time. The curves indicate a high dye adsorption rate during the first 15 min and a lower uptake rate thereafter, before reaching the equilibrium. Above the 42%, 36%, 18%, 25% and 24% of CR adsorption occurred in the first five min for CNiFe, $NiFeCO_3$, $NiAlCO_3$, $CoFeCO_3$ and $CoAlCO_3$ respectively (Fig. 13a). Thereafter, the rate of CR adsorption onto CNiFe and $NiFeCO_3$ LDH was found to be slow starting from 30 min with an uptake of 79% and 76% respectively. The equilibrium time of the CR sorption onto CNiFe was found to be at 60 min with an uptake percent of 100% against 65 min with an uptake percent of 97% in the original material (Fig. 13a). In general, it has been shown that calcined products CNiFe exhibit a high sorption capacity compared to uncalcined precursors. It can be explained by the increase of the surface area and surface basicity upon calcination. Fig. 13a display that the CR sorption decrease for $CoFeCO_3$ with very slowly rate than those for $CoAlCO_3$ and $NiAlCO_3$. It can be explained by the presence of impurities in the sample that can influence their adsorption site. The equilibrium time of the CR sorption onto $CoFeCO_3$ was found to be at 140 min with an uptake percent of 80% against 90 min with 92% and 120 min with 100%

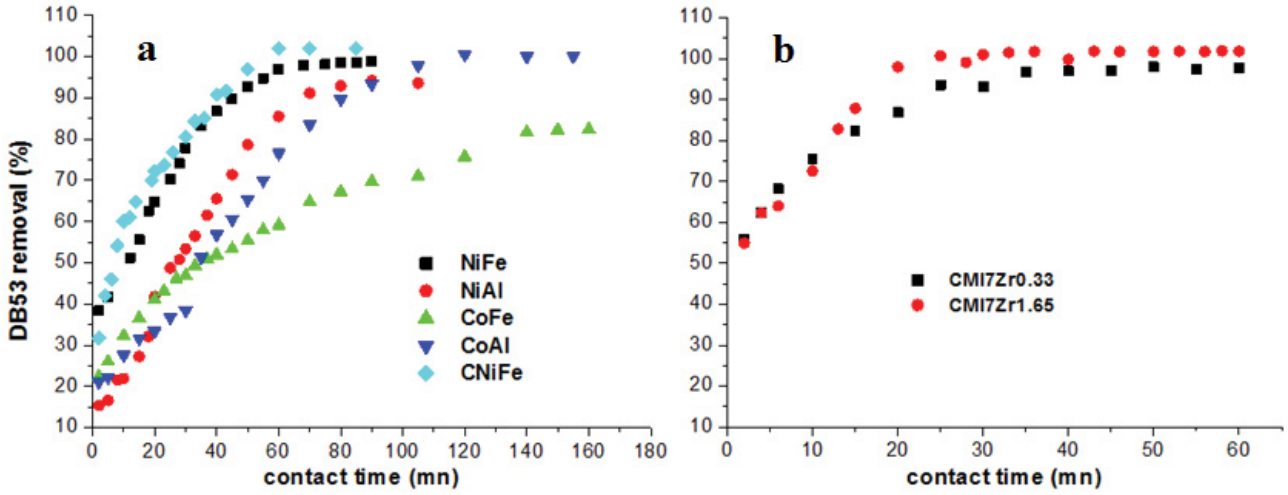

Fig. 13. Effect of contact time on the efficiency of CR removal from aqueous solution with concentration of the dye = 100 mg/L: (a) LDHs samples and (b) zirconia oxides samples.

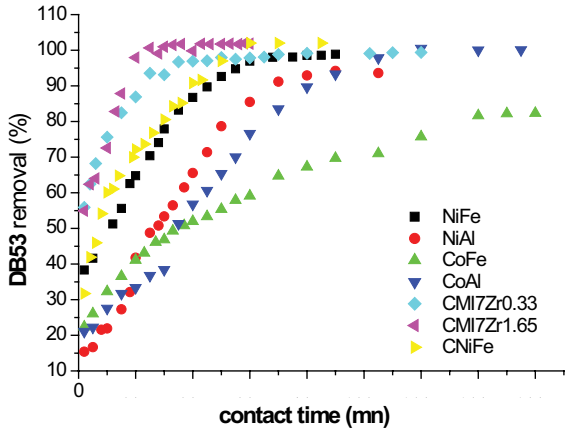

Fig. 14. Evaluation of CR dye removal efficiency by the as-synthesized materials.

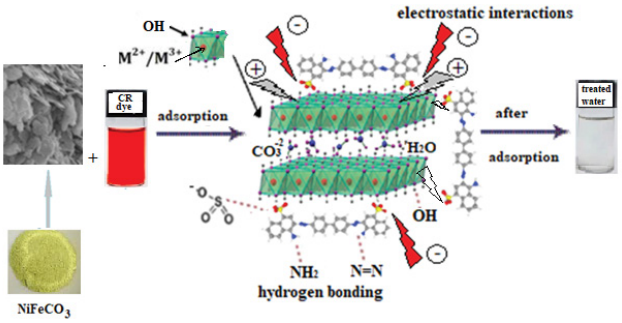

Fig. 15. Proposed schematic adsorption mechanism of CR dye on LDH materials.

onto $NiAlCO_3$ and $CoAlCO_3$ respectively (Fig. 13a). This suggests that the increase in CR uptake correlates with the crystallite size and better crystallinity for hydrotalcite.

Fig. 13b shows the adsorption properties of CR over the zirconia oxides (CMI7Zr0.33 and CMI7Zr1.65) as a function of time. The data clearly showed that zirconia oxide was more effective than LDHs for the removal of CR dye at the first minutes. It can be seen a higher adsorption capacity of the two samples. Above the 60% of CR sorption occurred in the first 5 min for the two zirconia materials. The adsorption of dye molecules over CMI7Zr1.65 was more rapid in comparison to CMI7Zr0.33 (Fig. 13b). It was showed that CMI7Zr0.33 exhibit a lower uptake rate there after starting from 20 min, with an uptake of 85% and reached the equilibrium time of the CR sorption at 35 min with an uptake percent of 95%. The sorption of the CR dye molecules over CMI7Zr1.65 remain rapid and reached the equilibrium time at 25 min with an uptake percent of 100%. Fig. 14 summarizes the main results obtained using these materials in environmental application that has been discussed in this article. This figure illustrates the efficiency of all materials synthetized. Fig. 14 shows that the adsorption of CR dye over zirconia oxides was more rapid [71] than LDH materials. The results reveal that the introduction of hierarchically porous structure into the zirconia materials improves the adsorption capacity in comparison to LDHs precursors. It was related to their macrochannels structure with mesoporous walls and high surface area.

3.5.3. Proposed mechanism of CR adsorption

Figs. 15 and 16 shows a schematic representation of the adsorption mechanism of CR onto LDHs and CMI7Zr respectively. In the case of LDHs (Fig. 15), CR dye can be

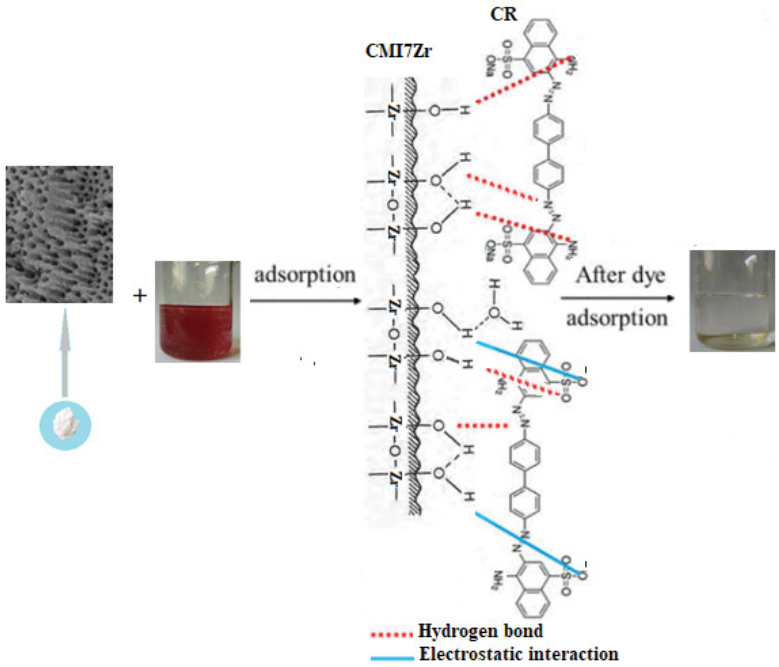

Fig. 16. Proposed schematic adsorption mechanism of zirconia oxide (CMI7Zr).

removed from solution by adsorption on the surface via electrostatic interaction between anionic sulfonate group ($-SO_3^-$) of CR and the positively charged surface of LDHs. Also present are hydrogen bonds between oxygen and the amino groups ($-NH_2$) of CR, oxygen, and the hydroxyl groups of the adsorbent [72]. Moreover, Fig. 16 shows the possible adsorption mechanisms of CR adsorption on zirconia oxide. We believed that the high and fast CR absorption ability of the CMI7Zr could be explained by: (1) the high surface area and high porosity, and (2) the CMI7Zr materials containing the hydroxyl group could effectively absorb the CR containing the amine group by the hydrogen bonding and may be trapped inside the pores (pore diffusion), which favored better adsorption of CR (Fig. 16).

4. Conclusion

We have synthesized a series of LDH materials with various combinations of transition metal cations, and molar ratios of divalent cation to trivalent cation equal to 3. Zirconia materials have been obtained via a sol-gel process using surfactant molecules ($C_{16}(EO)_{10}$) and zirconium n-butoxide as metal alkoxide precursor with two ratio 0.33 and 1.65. The synthesized materials have been tested for their sorption capabilities for Congo red dye (CR). It was discovered that $NiFeCO_3$ LDH exhibits a high and rapid sorption capability among all the LDHs materials tested. The sorption of CR dye molecules onto $CoFeCO_3$ was found to be very slowly. It has been shown that calcined LDH (CNiFe) exhibit the highest sorption capacity compared to uncalcined precursors. The study shows the highest sorption capacity of CR over the hierarchically porous zirconia materials with surfactant: Zr ratio (0.33 and 1.65) as a function of time. Otherwise, the sorption of dye molecules over CMI7Zr1.65 was slightly more rapid in comparison to CMI7Zr0.33. Moreover, the zirconia materials exhibit the better sorption capacity towards acidic dye molecules with a rapid removal in the initial stages and up to the first 15 min of contact, in comparison to the all HDLs products. The results reveal that the two porosities into the zirconia oxide structure and the highest surface area improve the sorption capacity. Therefore, the synthesized products can be considered as an effective sorbents for remediation of water contaminated from industrial effluents. Also, we believed that the process of adsorption is facilitated by various factors including, high surface area, high surface charge and high porosity.

Acknowledgments

The authors would like to gratefully acknowledge the Prof. Bao-Lian Su, Director, Laboratory of Inorganics Materials Chemistry (CMI), University of Namur, for providing facilities in carrying out this research and USTO-MB ORAN University for its financial support.

References

[1] G. Newcombe, Adsorption From Aqueous Solutions: Water Purification, Ed. Bottani, J.N. Tascón, Eds., Adsorption by Carbons, Elsevier, Amsterdam, 2008.
[2] Y. Omidi Khaniabadi, M. Javad Mohammadi, M. Shegerd, S. Sadeghi, S. Saeedi, H. Basiri, Removal of Congo red dye from aqueous solutions by a low-cost adsorbent: activated carbon prepared from *Aloe vera* leaves shell, Environ. Health Eng. Manage. J., 4 (2017) 29–35.
[3] L. Ai, J. Jiang, R. Zhang, Uniform polyaniline microspheres: a novel adsorbent for dye removal from aqueous solution, Synth. Met., 160 (2010) 762–767.
[4] J.N. Wekoye, W.C. Wanyonyi, P.T. Wangila, K.T. Mathew, Kinetic and equilibrium studies of Congo red dye adsorption on cabbage waste powder, Environ. Chem. Ecotoxicol., 2 (2020) 24–31.
[5] A. Musa, F. Al J. Maad, A.N. Laith, A.H.F. Ayad, Z. Hongshan, Al-A. Nadhir, N. Mu, Synthesis of a novel composite sorbent coated with siderite nanoparticles and its application for remediation of water contaminated with Congo red dye, Int. J. Environ. Res., 14 (2020) 177–191.
[6] P. Pengthamkeerati, T. Satapanajaru, O. Singchan, Sorption of reactive dye from aqueous solution on biomass fly ash, J. Hazard. Mater., 153 (2008) 1149–1156.
[7] W.C. Wanyonyi, J.M. Onyari, P.M. Shiundu, Adsorption of Congo red dye from aqueous solutions using roots of *Eichhornia crassipes*: kinetic and equilibrium studies, Energy Procedia, 50 (2014) 862–869.
[8] A.A. Adeyemo, I.O. Adeoye, O.S. Bello, Adsorption of dyes using different types of clay: a review, Appl. Water Sci., 20 (2015) 543–568.
[9] K.M. Parida, L. Mohapatra, Carbonate intercalated Zn/Fe, layered double hydroxide: a novel photocatalyst for the enhanced photo degradation of azo dyes, Chem. Eng. J., 179 (2012) 131–139.
[10] S. Yi, Z.H. Yang, S.W. Wang, D.R. Liu, S.Q. Wang, Q.Y. Liu, W.W. Chi, Effects of MgAlCe–CO_3 layered double hydroxides on the thermal stability of PVC resin, J. Appl. Polym. Sci., 119 (2011) 2620–2626.
[11] L. Yang, M. Dadwhal, Z. Shahrivari, M. Ostwal, P.K.T. Liu, M. Sahimi, T.T. Tsotsis, Adsorption of arsenic on layered double hydroxides: effect of the particle size, Ind. Eng. Chem. Res., 45 (2006) 4742–4751.
[12] G. Shiqing, K. Xiaonan, W. Lan, E. Lichtfouse, W. Chuanyi, Clay mineral adsorbents for heavy metal removal from wastewater: a review, Environ. Chem. Lett., 17 (2019) 629–654.
[13] G. Zhang, T. Wu, L. Li, X. Huang, Y. Wang, G. Wang, Sorption of humic acid to organo layered double hydroxides in aqueous solution, Chem. Eng. J., 191 (2012) 306–313.
[14] J. Yu, Q. Wang, D. O'Hare, L. Sun, Preparation of two dimentional layered double hydroxide nanosheets and their applications, Chem. Soc. Rev., 46 (2017) 5950–5974.
[15] T. Kawabata, Y. Shinozuka, Y. Ohishi, T. Shishido, K. Takaki, K. Takehira, Nickel containing Mg-Al hydrotalcite-type anionic clay catalyst for the oxidation of alcohols with molecular oxygen, J. Mol. Catal. A: Chem., 236 (2005) 206–215.
[16] S. Bouteraa, F.B.D. Saiah, S. Hamouda, N. Bettahar, Zn-M-CO_3 layered double hydroxides (M=Fe, Cr, or Al): synthesis, characterization, and removal of aqueous indigo carmine, Bull. Chem. React. Eng. Catal., 15 (2020) 43–54.
[17] K.H. Goh, T.T. Lim, Z. Dong, Application of layered double hydroxides for removal of oxyanions: a review, Water Res., 42 (2008) 1343–1368.
[18] D.G. Evans, X. Duan, Preparation of layered double hydroxides and their applications as additives in polymers as precursors to magnetic materials and in biology and medicine, Chem. Commun., 5 (2006) 485–496.
[19] A. Vaccari, Preparation and catalytic properties of cationic and anionic clays, Catal. Today, 41 (1998) 53–71.
[20] F. Boukraa Djellal Saiah, B.L. Su, N. Bettahar, Nickel–iron layered double hydroxide (LDH): textural properties upon hydrothermal treatments and application on dye sorption, J. Hazard. Mater., 165 (2009) 206–217.
[21] P. Kuśtrowski, D. Sułkowska, L. Chmielarz, A. Rafalska-Łasocha, B. Dudek, R. Dziembaj, Influence of thermal treatment conditions on the activity of hydrotalcite-derived Mg–Al oxides in the aldol condensation of acetone, Microporous Mesoporous Mater., 78 (2005) 11–22.
[22] L. El Gaini, M. Lakraimi, E. Sebbar, A. Meghea, M. Bakasse, Removal of indigo carmine dye from water to Mg-Al-CO_3-

calcined layered double hydroxides, J. Hazard. Mater., 161 (2009) 627–632.
[23] J. Orthman, H.Y. Zhu, G.Q. Lu, Use of anion clay hydrotalcite to remove coloured organics from aqueous solution, Sep. Purif. Technol., 31 (2003) 53–59.
[24] H. Zanhouane-Boudiaf, M. Boutahala, C. Tiar, L. Arab, F. Garin, Treatment of 2,4,5-trichlorophenol by MgAl-SDBS organo-layered double hydroxides: kinetic and equilibrium studies, Chem. Eng. J., 173 (2011) 36–41.
[25] Z.F. Ren, J. He, C.Q. Zhang, X. Duan Removal of chloride anion by calcined layered double hydroxides, Fine Chem., 19 (2002) 339–342.
[26] Y. Wang, C. Bryan, H. Gao, P. Pohl, C.J. Brinker, K. Yu, H. Xu, Y. Yang, P.S. Braterman, Z. Xu, Potential Applications of Nanostructured Materials in Nuclear Waste Management, United States: N. p., 2004.
[27] R. Birjega, O.D. Pavel, G. Costentin, M. Che, E. Angelescu, Rare-earth elements modified hydrotalcites and corresponding mesoporous mixed oxides as basic solid catalysts, Appl. Catal., A, 288 (2005) 93–185.
[28] R. Barrer, Zeolites and Clay Minerals as Sorbents and Molecular Sieves, Academic Press, London 1978.
[29] M. Hartmann, Ordered mesoporous materials for bioadsorption and biocatalysis, Chem. Mater., 17 (2005) 4577–4593.
[30] B. Smit, Molecular simulations of zeolites: adsorption, diffusion, and shape selectivity, Chem. Rev., 108 (2008) 4125–4184.
[31] X.Y. Li, L.H. Chen, Y. Li, J.C. Rooke, Z. Deng, Z.Y. Hu, J. Liu, A. Krief, X.Y. Yang, B.L. Su, Tuning the structure of a hierarchically porous ZrO_2 for dye molecule depollution, Microporous Mesoporous Mater., 152 (2012) 110–121.
[32] E.I. Kauppi, E.H. Rönkkönen, S.M.K. Airaksinen, S.B. Rasmussen, M.A. Bañares, A.O.I. Krause, Influence of H_2S on ZrO_2-based gasification gas clean-up catalysts: MeOH temperature-programmed reaction study, Appl. Catal., B, 111–112 (2012) 605–613.
[33] M. Labaki, H. Laversin, E.A. Zhilinskaya, A. Aboukaïs, D. Courcot, Electron paramagnetic resonance investigation of the nature of active species involved in carbon black oxidation on ZrO_2 and Cu/ZrO_2 catalysts, Catal. Commun., 17 (2012) 64–70.
[34] X. Zhang, H. Su, X. Yang, Catalytic performance of a three-dimensionally ordered macroporous Co/ZrO_2 catalyst in Fischer–Tropsch synthesis, J. Mol. Catal. A: Chem., 360 (2012) 16–25.
[35] M. Signoretto, F. Menegazzo, L. Contessotto, F. Pinna, M. Manzoli, F. Boccuzzi, Au/ZrO_2 an efficient and reusable catalyst for the oxidative esterification of renewable furfural, Appl. Catal., B, 129 (2013) 287–293.
[36] A.A. Ashkarran, S.A.A. Afshar, S.M. Aghigh, M. Kavianipour, Photocatalytic activity of ZrO_2 nanoparticles prepared by electrical arc discharge method in water, Polyhedron, 29 (2010) 1370–1374.
[37] A.B. Nawale, N.S. Kanhe, S.V. Bhoraskar, V.L. Mathe, A.K. Das, Influence of crystalline phase and defects in the ZrO_2 nanoparticles synthesized by thermal plasma route on its photocatalytic properties, Mater. Res. Bull., 47 (2012) 3432–3439.
[38] T. Liu, L. Li, L. Yu, An electrochemical sulfur sensor based on ZrO_2(MgO) as solid electrolyte and ZrS_2 + MgS as auxiliary electrode, Sens. Actuators, B, 139 (2009) 501–504.
[39] R. Zhang, X. Zhang, S. Hu, High temperature and pressure chemical sensors based on Zr/ZrO_2 electrode prepared by nanostructured ZrO_2 film at Zr wire, Sens. Actuators, B, 149 (2010) 143–154.
[40] A. Vantomme, A. Léonard, Z.Y. Yuana, B.L. Su, Self-formation of hierarchical micro-meso-macroporous structures: generation of the new concept "Hierarchical Catalysis", Colloids Surf., A, 300 (2007) 70–78.
[41] J.L. Blin, L. Gigot, A. Léonard, B.L. Su, Synthesis and characterization of nanostructured mesoporous zirconia catalyst supports using non-ionic surfactants as templating agents, Stud. Surf. Sci. Catal., 143 (2002) 1035–1043.
[42] J.L. Blin, L. Gigot, A. Léonard, B.L. Su, Mesoporous zirconium oxides: an investigation of physico-chemical synthesis parameters, Stud. Surf. Sci. Catal., 141 (2002) 257–264.
[43] J.L. Blin, A. Léonard, G. Laurent, P. Olivier, B.L. Su, Nanostructured mesoporous TiO_2, ZrO_2 and SiO_2 synthesis by using the non-ionic $C_m(EO)_n$ - inorganic alkoxyde system: toward a better understanding on the formation mechanism, Stud. Surf. Sci. Catal., 146 (2003) 443–446.
[44] Y.M. Zheng, S.F. Lim, J.P. Chen, Preparation and characterization of zirconium-based magnetic sorbent for arsenate removal, J. Colloid Interface Sci., 338 (2009) 22–29.
[45] K. Okrovski, K.T. Jung, A.T. Bell, Investigation of CO and CO_2 adsorption on tetragonal and monoclinic zirconia, Langmuir, 17 (2001) 4297–4303.
[46] V. Hornebecq, C. Knofel, P. Boulet, B. Kuchta, L.P. Llewellyn, Adsorption of carbon dioxide on mesoporous zirconia: microcalorimetric measurements, adsorption isotherms modelling and density-functional theory calculations, J. Phys. Chem. C, 115 (2011) 10097–10103.
[47] R.F.D. Farias, A.A.S. Do Nascimento, C.W.B. Bezerra, Adsorption of Co(II), Ni(II), Cu(II), and Zn(II) on hexagonal templated zirconia obtained thorough a sol–gel process: the effects of nanostructure on adsorption features, J. Colloid Interface Sci., 277 (2004) 19–22.
[48] P. Nayak, B.B. Nayak, A. Mondal, Surfactant assisted synthesis of high surface area ceria modified mesoporous tetragonl zirconia powder and its chromium adsorption study, Mater. Chem. Phys., 127 (2001) 12–15.
[49] C. Morterra, G. Meligrana, G. Cerrato, V. Solinas, E. Rombi, M.F. Sini, 2,6-Dimethylpyridine adsorption on zirconia and sulfated zirconia systems. An FTIR and microcalorimetric study, Langmuir, 19 (2003) 5344–5356.
[50] P.A. Deshpande, S. Polisetti, G. Madras, Rapid synthesis of ultrahigh adsorption capacity zirconia by a solution combustion technique, Langmuir, 2 (2011) 3578–3587.
[51] Q. Luo, L. Li, B. Yang, D. Zhao, Three-dimensional ordered macroporous structures with hexagonal mesoporous silica walls, Chem. Lett., 4 (2000) 378–379.
[52] T. Sen, G.J.T. Tiddy, J.L. Casci, M.W. Anderson, One-pot synthesis of hierarchically ordered porous silica materials on three orders of length scale, Chem. Int. Ed., 42 (2003) 4649–4653.
[53] A. Imhof, D.J. Pine, Ordered macroporous materials by emulsion templating, Nature, 389 (1997) 948–951.
[54] D.M. Antonelli, Synthesis of macro-mesoporous niobium oxide molecular sieves by a ligand-assisted vesicle templating strategy, Microporous Mesoporous Mater., 33 (1999) 209–214.
[55] W. Deng, M.W. Toepke, B.H. Shanks, Surfactant-assisted synthesis of alumina with hierarchical nanopores, Adv. Funct. Mater., 13 (2003) 61–65.
[56] J.L. Blin, A. Leonard, Z.Y. Yuan, L. Gigot, L. Vantomme, A.K. Cheetham, B.L. Su, Hierarchically mesoporous/macroporous metal oxides templated from polyethylene oxide surfactant assemblies, Angew. Chem. Int. Ed., 42 (2003) 2872–2875.
[57] Z.Y. Yuan, A. Vantomme, A. Leonard, B.L. Su, Surfactant-assisted synthesis of unprecedented hierarchical meso-macrostructured zirconia, Chem. Commun., 9 (2003) 1558–1559.
[58] A. Vantomme, Z.Y. Yuan, B.L. Su, One-pot synthesis of a high-surface-area zirconium oxide material with hierarchically three-length-scaled pore structure, New J. Chem., 28 (2004) 1083–1085.
[59] Z.Y. Yuan, T.Z. Ren, A. Vantomme, B.L. Su, Facile and generalized preparation of hierarchically mesoporous–macroporous binary metal oxide materials, Chem. Mater., 16 (2004) 5096–5106.
[60] A. Léonard, J.L. Blin, B.L. Su, One-pot surfactant assisted synthesis of alumino silicate macrochannels with tunable micro-or mesoporous wall structure, Chem. Commun., 9 (2003) 2568–2569.
[61] R.M. Ormerod, Solid oxide fuel cells, Chem. Soc. Rev., 32 (2003) 17–28.
[62] D. Prahas, Y. Kartika, N. Indraswati, S. Ismadji, Activated carbon from jackfruit peel waste by H_3PO_4 chemical activation: pore structure and surface chemistry characterization, Chem. Eng. J., 140 (2008) 32–42.
[63] Q. Liu, L.B. Zhong, Q.B. Zhao, C. Frear, Y.M. Zheng, Synthesis of Fe_3O_4/polyacrylonitrile composite electrospun nanofiber

mat for effective adsorption of tetracycline, ACS Appl. Mater. Interfaces, 7 (2015) 14573–14583.
[64] JCPDS: Joint Committee on Powder Diffraction Standards, International Centre for Diffraction Data, Pennsylvania, U.S.A., 1977.
[65] E.P. Barrett, L.G. Joyner, P.P. Halenda, The determination of pore volume and area distributions in porous substances. I. computations from nitrogen isotherms, J. Am. Chem. Soc., 73 (1951) 373–380.
[66] E.C. Kruissink, L.J.V. Reijden, J.R.H. Ross, Co-precipitated nickel-alumina catalysts for methanation at high temperature, Part 1. Chemical composition and structure of the precipitates, J. Chem. Soc. Faraday Trans., 77 (1981) 649–663.
[67] A.A. Mohammed, Biosorption of lead, cadmium and zinc onto sunflower shell equilibrium, kinetic and thermodynamic studies, Iraqi J. Chem. Pet. Eng., 16 (2015) 91–105.
[68] M.K. Purkait, A. Maiti, S. Das Gupta, S. De, Removal of Congo red using activated carbon and its regeneration, J. Hazard. Mater., 145 (2007) 287–295.
[69] V.S. Munagapati, D. Kim, Adsorption of anionic azo dye Congo red from aqueous solution by cationic modified orange peel powder, J. Mol. Liq., 220 (2016) 540–548.
[70] Z. Esvandi, R. Foroutan, S.J. Peighambardoust, A. Akbari, B. Ramavandi, Uptake of anionic and cationic dyes from water using natural clay and clay/starch/$MnFe_2O_4$ magnetic nanocomposite, Surf. Interfaces, 21 (2020) 100754, doi: 10.1016/j.surfin.2020.100754.
[71] J. Pan, J. Zeng, Q. Cao, H. Gao, Y. Yan, Hierarchical macro and mesoporous foams synthesized by HIPEs template and interface grafted route for simultaneous removal of λ-cyhalothrin and copper ions, Chem. Eng. J., 284 (2016) 1361–1372.
[72] C. Prasad, H. Tang, Q.Q. Liu, S. Zulfiqar, S. Shah, I. Bahadur, An overview of semiconductors/layered double hydroxides composites: properties, synthesis, photocatalytic and photoelectrochemical applications, J. Mol. Liq., 289 (2019) 111114, doi: 10.1016/j.molliq.2019.111114.